JOURNAL OF APPLIED PHYSICS VOLUME 86, NUMBER 1 1 JULY 1999

Representation of GaP formation by a reduced order surface kinetics model using *p*-polarized reflectance measurements

S. Beeler[a] and H. T. Tran
Center for Research in Scientific Computation and Department of Mathematics, North Carolina State University, Box 8205, Raleigh, North Carolina 27695

N. Dietz[b]
Departments of Physics and Materials Science, North Carolina State University, Box 7919, Raleigh, North Carolina 27695

(Received 11 December 1998; accepted for publication 1 April 1999)

This contribution presents results on the parameter estimation of rate constants and optical response factors in a reduced order surface kinetics (ROSK) model, which has been developed to describe the decomposition kinetics of the organometallic precursors involved and their incorporation into the film deposition. As a real-time characterization technique, we applied *p*-polarized reflectance spectroscopy (PRS) during low temperature growth of epitaxial GaP heterostructures on Si(001) substrates by pulsed chemical beam epitaxy. The high surface sensitivity of PRS allows us to follow alterations in the composition and thickness of the surface reaction layer as they are encountered during periodic precursor supply. Linkage of the PRS response to the ROSK model provides the base for the parameter estimation of the reduced order surface kinetics model, giving insights into the organometallic precursor decomposition and growth kinetics. © *1999 American Institute of Physics.* [S0021-8979(99)07713-0]

I. INTRODUCTION

Low pressure deposition methods, such as chemical beam epitaxy (CBE) and plasma enhanced chemical vapor deposition, play an important role in the manufacturing of nanostructure devices and advanced ultralarge-scale integration (ULSI) processing, respectively. Some areas of interest are novel quantum well electronic devices, improved densities of integrated electronic devices, methods of improving the control of epitaxial deposition to realize these devices, the efficacy of resonant tunneling devices with respect to speed and reduced power, and demonstrated techniques for monolithic and hybrid integration of devices based on gallium arsenide (GaAs), indium phosphide (InP),[1] and silicon.[2] Key targets in III-V compound/silicon heterostructures are the understanding and control of defect formation as well as the interactions and propagation of defects during later stages of compound heteroepitaxy growth. These are intimately linked to the understanding and control of the kinetics of heteroepitaxy, which in turn is closely related to the surface structure that depends on both the reconstruction and the nature and distribution of defects in the epitaxial film. However, progress in understanding and controlling thin film growth has been very slow, because little is known about chemical reaction pathways and reaction kinetics parameters during the decomposition process of metalorganic (MO) precursors. Furthermore, stringent tolerances in the engineering of advanced optoelectronic integrated circuits with respect to controlled thickness and composition of ultrathin layers require the development of monitoring and control techniques that follow the deposition process with submonolayer resolution. These demands led to the development of surface-sensitive real-time optical sensors[3] that are able to move the monitoring and control point close to the point where the growth occurs, which in a chemical beam epitaxy process is the surface reaction layer, which is built up by physisorbed and chemisorbed precursor fragments between the ambient and the film interface.

Applying optical probe techniques to real-time characterization of thin film growth carries with it the challenge of relating surface chemistry processes that drive the growth process to growth/film properties, such as composition, instantaneous growth rate or structural layer quality. As illustrated in Fig. 1, in deposition four primary regions are involved. Presently most characterization techniques are aimed towards accurately measuring ambient process parameters, such as pressure, flux or temperature, since numerous probes are available to provide a relatively detailed assessment of the ambient. This strategy is clearly limited in its capability to deal with complex nonlinear surface chemistry processes, where the surface plays an integral role in the precursor decomposition pathways and small changes in the ambient composition can affect the growth substantially.

During the last few years, we developed and explored *p*-polarized reflectance spectroscopy (PRS)[4–6] as a highly surface-sensitive sensing technique, which allows us to follow the surface reaction kinetics under steady-state growth conditions. Utilizing this knowledge, we presently are exploring its application towards closed-loop control of deposition processes at low pressure (PCBE).[7]

First, in Sec. II we will give a brief background on the experimental growth and monitoring conditions and show results obtained by PRS during real-time characterization of heteroepitaxial growth of GaP on Si substrates. In Sec. III we introduce the model used to simulate the PRS measurements.

[a]Electronic mail: scbeeler@eos.ncsu.edu
[b]Electronic mail: ndietz@unity.ncsu.edu

 © 1999 American Institute of Physics

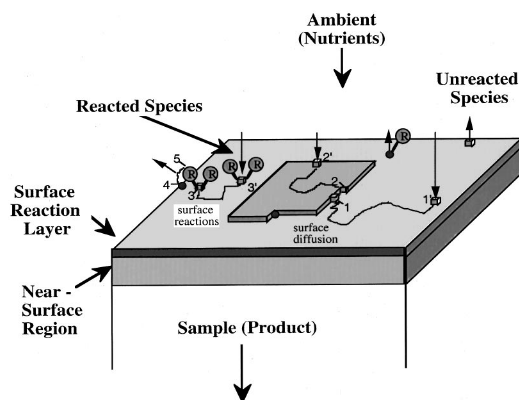

FIG. 1. The four primary regions involved in deposition are (1) the ambient; (2) the surface reaction layer, which consists of species physisorbed or chemisorbed to the surface in dynamic equilibrium with both ambient and surface; (3) the surface itself; and (4) the near-surface region that can be defined as consisting of the outermost several atomic layers of the fabricated sample.

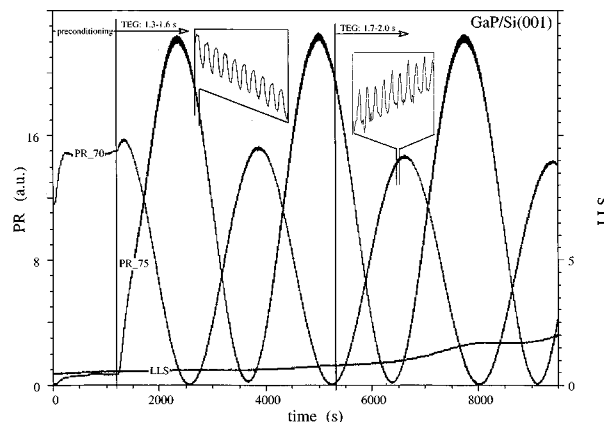

FIG. 3. Monitoring of heteroepitaxial GaP growth under PCBE growth conditions by PRS and LLS. The insets show enlargements of the PR responses to periodically modulated SRL composition and thickness during pulsed precursor supply.

We describe there the link of the PR response to the simulation parameters accessible through the reduced order surface kinetics (ROSK) model, which has been developed to describe the decomposition kinetics of the involved organometallic precursors.[7] The process of identifying these parameters is explained in Sec. IV, and in Sec. V the results of the parameter identification are analyzed. The knowledge gained from the ROSK model allows us to establish and validate surface reaction kinetics parameters, thus advancing our understanding of fundamental chemistry processes in thin film growth processes using organometallic precursors. Finally, our concluding remarks are contained in Sec. VI.

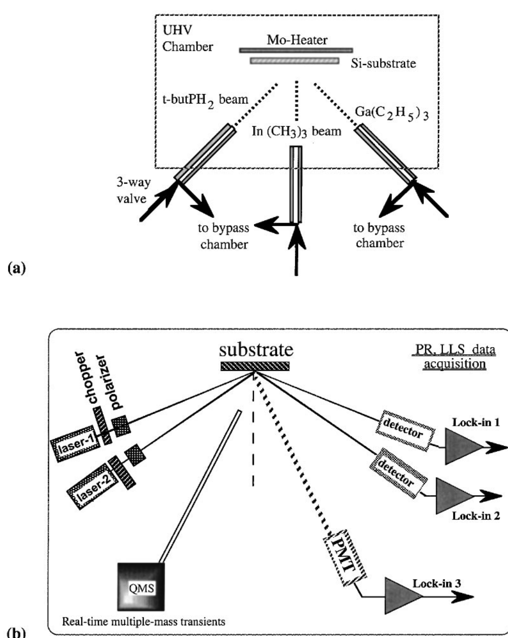

FIG. 2. (a) Setup of the PCBE system for III-V compound semiconductor growth; (b) schematic setup of growth monitoring by PRS, LLS and quadrupole mass spectroscopy (QMS).

II. EXPERIMENTAL SETUP AND RESULTS

For monitoring both the bulk and surface properties during heteroepitaxial GaP growth on Si, PRS has been integrated into a pulsed CBE (PCBE) system schematically shown in Fig. 2(a). In PCBE, the surface of the substrate is exposed to pulsed ballistic beams of $[(C_4H_9)PH_2]$ (TBP) and $[Ga(C_2H_5)_3]$ (TEG) at typically 350–450 °C to accomplish nucleation and overgrowth of the silicon by an epitaxial GaP film. For PRS and laser light scattering (LLS) we employ *p*-polarized light beams at two angles of incidence (PR70: $\varphi=71.5°$ and PR75: $\varphi=75.2°$) using the wavelength $\lambda=632.8$ nm and Glan-Thompson prisms, as illustrated in Fig. 2(b). Further details on the experimental conditions are given in previous publications.[4–17]

During the preconditioning period, the PR signals change according to the temperature dependence of the substrate dielectric function. The PR signals are used to verify independent temperature measurements and to calibrate the actual surface temperature. A constant flow of palladium purified H_2 (10 sccm) is introduced into the growth chamber during the preconditioning as well as during the growth period. The background pressure in the growth system is $<1\times10^{-9}$ Torr and it increases to 5×10^{-5} Torr during pregrowth and to 2×10^{-4} Torr during growth.

Figure 3 shows the PR and LLS signals during heteroepitaxial growth of GaP on Si(001). After initiating growth at 1200 s, minima and maxima are observed in the time evolution of the PR signals due to interference phenomena as the film grows. It should be noted that the maxima and minima of the two signals are inverted, which is due to the fact that one angle of incidence (PR75) is above—and the other (PR70) below—the pseudo-Brewster angle of the growing film. Superimposed on the interference oscillations of the reflectance is a fine structure that is strongly correlated to the time sequence of the supply of precursors employed during the steady-state growth conditions. The two insets in Fig. 3 show enlargements of the fine structure evolutions for 30 s of growth for PR75 and PR70, respectively.

For the surface reaction kinetics analysis and the validation of simulations performed using the ROSK model pre-

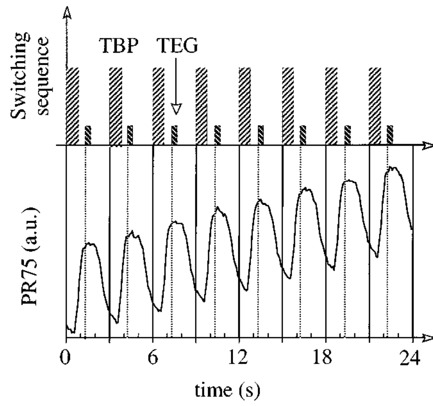

FIG. 4. PR75 response to periodic exposure of growth surface to TBP and TEG precursor pulses, taken at the rising flank of an interference fringe. The total cycle time is 3 s with TPB pulses from 0 to 0.8 s and TEG pulses from 1.3 to 1.6 s.

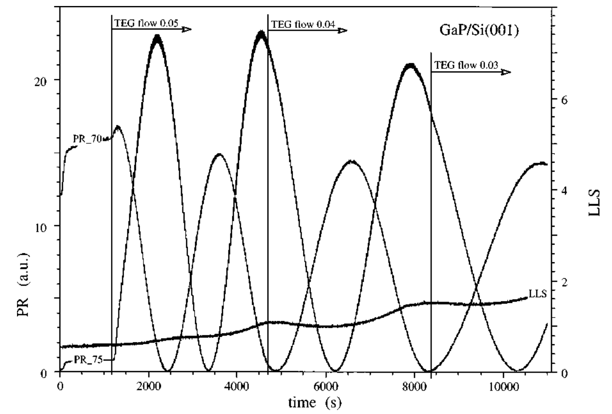

FIG. 6. PRS and LLS responses during heteroepitaxial GaP growth under PCBE growth, where at the positions marked the flow rate of TEG was changed, thus maintaining the pulse switching pattern for the supplied precursors.

sented later in the article, we varied two experimental parameters: (i) the position of the TEG pulse of 300 ms length within the precursor cycle sequence and (ii) the TEG flow rate. One growth condition was carried and monitored for at least one and a half interference oscillations in order to get stable steady-state growth and to gather sufficient information to analyze and simulate the growth process.

The correlation of the fine structure evolution with the pulsing sequence of the precursor supply is shown in more detail in Fig. 4. In Fig. 4, the PR response is taken during steady-state growth on a rising flank of an interference fringe using a pulse cycle sequence of 3 s, a TBP pulse from 0.0 to 0.8 s, a TEG pulse from 1.3 to 1.6 s and continuous hydrogen flow during the complete sequence. In the first set of experiments, the flow rates and pulse durations of TBP (800 ms at 0.907 sccm, starting at 0.0 s) and TEG (300 ms at 0.04 sccm) were kept constant and only the start position of the TEG pulse was varied from 0.9 to 2.3 s. The effect on the fine structure evolution is shown in Fig. 5, where the starting point of the TEG pulse is marked by an arrow. This influence of TEG pulse position on the PR response will be explained more fully in Sec. V. For comparison, all PR responses are taken at the same intensity/reflectance level on a rising flank of an interference oscillation. We note that the exposure times as well as the precursor fluxes are identical for each trace shown in Fig. 5.

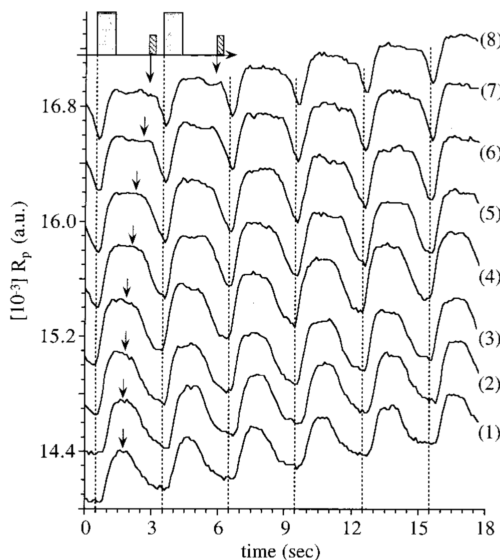

FIG. 5. PR75 responses for various TEG positions within a cycle sequence. The TBP exposure time, position and flux were kept constant. The flux and surface exposure time to TEG were constant; only the start point (marked by an arrow) was changed. The TEG positions used were in steps of 0.2 s from (1) 0.9 to 1.2 up to (8) 2.3 to 2.6 s.

In the second set of experiments, the changes in surface reaction kinetics and growth are evaluated for TBP:TEG flow ratios between 18 and 30. Figure 6 shows the PR and LLS signals during heteroepitaxial growth of GaP on Si(001) for three TEG flow settings of 0.05, 0.04 and 0.03 sccm, with a TBP pulse of 0.0–0.8 s (at 0.907 sccm) and a TEG pulse of 1.3–1.6 s, in a pulse cycle sequence of 3 s. With decreasing TEG flow, the spacing of the interference oscillations widens according to the reduced growth rate. More details including comparisons with the results of simulations are given in Sec. V.

III. MODELING OF PRS RESULTS

We represent the structure of the chemical vapor deposition of a growing heteroepitaxial film with a four-layer medium model consisting of (1) ambient, (2) a surface reaction layer (SRL), (3) film and (4) substrate. We consider here GaP film growth on a Si substrate. The complex reflectivity coefficient for p-polarized incident light, given a four-layer stack, is[18]

$$r_p=\frac{r_{12}(1+r_{23}r_{34}e^{-2i\beta_3})+(r_{23}+r_{34}e^{-2i\beta_3})e^{-2i\beta_2}}{(1+r_{23}r_{34}e^{-2i\beta_3})+r_{12}(r_{23}+r_{34}e^{-2i\beta_3})e^{-2i\beta_2}}, \quad (3.1)$$

where the Fresnel coefficients $r_{k(k+1)}$ ($k=1$, 2, and 3) for interfaces 1-2, 2-3, and 3-4 are given by[19]

$$r_{k(k+1)}=\frac{\epsilon_{k+1}\sqrt{\epsilon_k-\epsilon_1\sin^2\phi_1}-\epsilon_k\sqrt{\epsilon_{k+1}-\epsilon_1\sin^2\phi_1}}{\epsilon_{k+1}\sqrt{\epsilon_k-\epsilon_1\sin^2\phi_1}+\epsilon_k\sqrt{\epsilon_{k+1}-\epsilon_1\sin^2\phi_1}}, \quad (3.2)$$

and the phase shifts β_k for the SRL ($k=2$) and the growing film ($k=3$) are given by

$$\beta_k = \frac{2\pi}{\lambda} d_k \sqrt{\epsilon_k - \epsilon_1 \sin^2 \phi_1}. \tag{3.3}$$

Using Eqs. (3.1)–(3.3), the reflectivity coefficient r_p is a function of d_2 and d_3 (the thicknesses of the SRL and the film, respectively), ϵ_1, ϵ_2, ϵ_3 and ϵ_4 (the complex dielectric functions of the ambient, SRL, film and substrate, respectively), and ϕ_1 and λ. Here, ϕ_1 denotes the angle of incidence and λ is the wavelength of the impinging laser light.[8]

The values of ϵ_1, ϵ_3, ϵ_4, ϕ_1 and λ are constant in time, but ϵ_2, d_2 and d_3 vary in time as the film grows and the SRL composition and thickness change. To understand how these values change, we need a representative model of the chemical kinetics of the SRL, which approximates the pyrolysis of the primary source molecules and has been discussed in detail elsewhere.[20–22] For TBP and TEG as source vapors forming GaP, we employed a ROSK[7] model. The ROSK model makes the simplifying assumption that the many reactions which make up the TBP pyrolysis are combined into one step, the reactions which make up the TEG decomposition are combined into two steps, and the formation of GaP is one final step. The process is driven by a periodic source vapor cycle as described in Sec. V.

Thus the kinetic model representing the SRL reactions is given by the following system of ordinary differential equations:

$$\frac{d}{dt} n_1(t) = S_1(t) - k_1 n_1(t) - k_{\mathrm{GaP}} n_1(t) n_3(t), \tag{3.4}$$

$$\frac{d}{dt} n_2(t) = S_2(t) - k_2 n_2(t) - k_3 n_2(t), \tag{3.5}$$

$$\frac{d}{dt} n_3(t) = k_3 n_2(t) - k_4 n_3(t) - k_{\mathrm{GaP}} n_1(t) n_3(t), \tag{3.6}$$

$$\frac{d}{dt} n_4(t) = k_{\mathrm{GaP}} n_1(t) n_3(t). \tag{3.7}$$

The variables n_1, n_2 and n_3 represent the number of moles of the components of the SRL: active surface phosphorus fragments, diethylgallium (DEG), and monoethylgallium (MEG) and active gallium fragments, respectively. In Eq. (3.4) the change in active phosphorus fragments is written as a sum of a source term S_1, a desorption loss term $-k_1 n_1$ and a reaction term forming GaP. The second equation, Eq. (3.5), which describes the defragmentation of TEG, contains a source term S_2, a desorption loss term $-k_2 n_2$ and a term of decomposition into MEG and active gallium fragments. Equation (3.6) (change in MEG and active surface gallium fragments) has a term of creation, a desorption loss term and a reaction term forming GaP. The fourth variable, n_4, Eq. (3.7), represents the numbers of moles of created GaP integrated into the deposited GaP film layer. This equation contains only the single reaction term for the formation of GaP from active surface Ga and P and has to also account for any surface activation processes.

The source terms in the differential equations are based on the source vapor pulses. More specifically, we modeled the source terms by the following expression:

$$S_1(t) = \frac{P_1(t) \gamma \beta_{\mathrm{TBP}}}{V_{\mathrm{TBP}}}, \tag{3.8}$$

where $P_1(t)$ is the source vapor flow rate. V_{TBP} is the molar volume of TBP and the constant β_{TBP} is the sticking coefficient of TBP. The geometrical parameter γ represents how much of the source vapors actually hits the surface of the wafer (a constant dependent on the structure of the reactor). Similarly, the second source term is represented by

$$S_2(t) = \frac{P_2(t) \gamma \beta_{\mathrm{TEG}}}{V_{\mathrm{TEG}}}, \tag{3.9}$$

with corresponding $P_2(t)$, V_{TEG} and β_{TEG} for the TEG pulse, and the same constant γ. For each source term we are using a constant flow rate between the start and stop times (and zero flow elsewhere), as described in Sec. II. There is a small time difference between the switching on (or off) of the pulse and the start (or stop) of the source vapors at the surface. This is caused by the time needed for the source vapor gates to open or close and for the vapors to travel to the surface. We account for it with a parameter *delay*, so that for a source vapor pulse set to start at t_{on} and stop at t_{off}, the source vapors will actually reach the surface starting at $t_{\mathrm{on}} + \mathrm{delay}$ and stopping at $t_{\mathrm{off}} + \mathrm{delay}$. The delay was estimated to be 0.72 s using a parameter identification process that is described in Sec. IV.

The system of differential equations (3.4)–(3.7), together with the source terms, Eqs. (3.8) and (3.9), and appropriate initial conditions, can be solved numerically for the number of moles n_1, n_2, n_3 and n_4. From these solutions, the film and SRL thicknesses are found by the following equations:

$$d_3(t) = \frac{V_{\mathrm{GaP}}}{A} n_4(t), \tag{3.10}$$

$$d_2(t) = \frac{\alpha_{\mathrm{SRL}}}{A} [V_1 n_1(t) + V_2 n_2(t) + V_3 n_3(t)], \tag{3.11}$$

and the effective dielectric function of the SRL is given by

$$\epsilon_2(t) = 1 + \left[\frac{n_1(t)}{\sum_{k=1}^3 n_k(t)} F_1 + \frac{n_2(t)}{\sum_{k=1}^3 n_k(t)} F_2 + \frac{n_3(t)}{\sum_{k=1}^3 n_k(t)} F_3 \right], \tag{3.12}$$

which is derived from the Sellmeier equation.[23] In the above three equations, A is the surface area of the wafer, the values V_k are the molar volumes of the components n_k, and V_{GaP} is the molar volume of GaP. The parameters F_k are the optical responses of the components of the SRL and α_{SRL} is an effective SRL thickness parameter representing the percentage of the SRL that contributes to the reflectance behavior. With the values of the temporal dependent parameters ϵ_2, d_2 and d_3 found by Eqs. (3.10)–(3.12), and with the constant parameters ϵ_1, ϵ_3, ϵ_4, ϕ_1 and λ, the reflectivity coefficient r_p can be computed from Eqs. (3.1)–(3.3). From r_p, we then find the value that is actually measured in the experiments by computing the reflectance $R_p = |r_p|^2$.

In the equations described here in Sec. III, $\phi_1, \lambda, \epsilon_1, V_1, V_2, V_3, V_{\mathrm{GaP}}, V_{\mathrm{TBP}}, V_{\mathrm{TEG}}, A, \beta_1, \beta_2, \alpha_{\mathrm{SRL}}$, all start/stop times, and flow rates contributing to P_1 and P_2 are

known quantities. The values of the dielectric functions ϵ_3 and ϵ_4, the rate constants k_1, k_2, k_3, k_4 and k_{GaP}, the optical responses F_1, F_2 and F_3, the geometrical parameter γ, and *delay* are not known. Our work in Secs. IV and V is to find values of these parameters so that the mathematical model most closely matches experimental results.

IV. PARAMETER IDENTIFICATION PROBLEM

Here we formulate the inverse least squares problem used to find the set of parameters with which the results of the mathematical model of the reflectance (described in Sec. III) match most closely with the experimental data. More specifically, we are looking for the vector of parameters $\vec{q}=(F_1,F_2,F_3,k_1,k_2,k_3,k_4,k_{\mathrm{GaP}},\gamma,\mathrm{delay})$ that minimizes the following cost function:

$$J(\vec{q})=\sqrt{\sum_i \left(R_{\mathrm{expt}}(t_i)-R_{\mathrm{calc}}(t_i,\vec{q})\right)^2}. \tag{4.1}$$

Here $R_{\mathrm{expt}}(t_i)$ is the experimental data set at the measurement times t_i and $R_{\mathrm{calc}}(t_i,\vec{q})$ is the simulation results calculated at the same times using the parameter set $\vec{q}$.

We do not include ϵ_3 and ϵ_4 in $\vec{q}$, because larger numbers of parameters make the minimization process increasingly difficult. We can remove these two parameters from the above parameter estimation problem by formulating a separate but simpler estimation problem. In particular, we use a three-layer stack as a simpler model of the growing film: removing the SRL from consideration leaves just the ambient, the film and substrate layers. The formula for calculating the reflectance for a three-layer stack analytically is given by

$$r_{3,p}=\frac{r_{13}+r_{34}e^{-2i\beta_3}}{1+r_{13}r_{34}e^{-2i\beta_3}}, \tag{4.2}$$

where r_{13} and r_{34} are Fresnel coefficients for the reflection from interfaces 1-3 and 3-4 (now that layer 2 is removed), and the phase shift β_3 is for the film layer. These values are calculated by formulas analogous to Eqs. (3.2) and (3.3).

To compare results from this formula with experimental results, we first remove the effects of the SRL from the experimental data by removing the small-amplitude fine structure oscillations modulated with the precursor cycle from the large-amplitude interference oscillations, which have a periodicity of several hundreds of seconds. In order to remove the fine structure, first the curves on either side of the data forming an envelope around it must be found. The experimental version of the three-layer stack reflectance is then found by switching from one side of the envelope to the other where the fine structure ''turns'' from positive to negative (from adding to the three-layer stack reflectance to subtracting from it) or vice versa. This orientation of the fine structure is cyclical with the interference oscillations, either turning twice per oscillation or else not turning at all, in which case there is no switching between envelope sides. Figure 7 shows this extraction of the three-layer reflectance out of the experimental data near a turning point. The three-layer reflectance plus the minimal influence from the SRL during a cycle is shown on one side of the data (switching sides at the turning point), while the other side represents the three-layer stack plus the maximal influence from the SRL during the cycle.

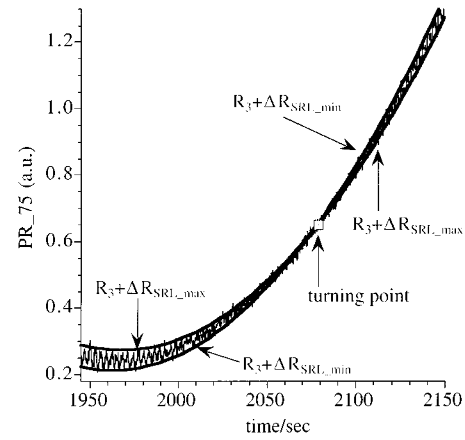

FIG. 7. Extraction of envelope reflectance spectra from PR75 data by removing the fine structure, shown near a turning point.

With this method of extracting the experimental three-layer stack reflectance $R_{3,\mathrm{expt}}$, we can identify the parameters ϵ_3 and ϵ_4, as well as an average growth rate $\hat{g}_r$ (used to find the film thickness at times t_i), by comparing the calculated reflectance $R_{3,\mathrm{calc}}=|r_{3,p}|^2$ from Eq. (4.2) to $R_{3,\mathrm{expt}}$. This is done also through an inverse least squares formulation by finding $\vec{r}=(\epsilon_3,\epsilon_4,\hat{g}_r)$ that minimizes the cost function

$$J(\vec{r})=\sqrt{\sum_i \left(R_{3,\mathrm{expt}}(t_i)-R_{3,\mathrm{calc}}(t_i,\vec{r})\right)^2}. \tag{4.3}$$

Once the values of ϵ_3 and ϵ_4 are found, they can be used in solving the four-layer stack parameter identification problem to find the unknown parameters $F_1,F_2,F_3,k_1,k_2,k_3,k_4,k_{\mathrm{GaP}},\gamma$, and *delay*.

V. ANALYSIS OF RESULTS

Comparing measurements taken with the TEG pulse position varied while all other conditions are fixed (see, e.g., the fine structure shown in Fig. 5) reveals several important characteristics in the fine structure. We will explain these features and show how the mathematical simulation of the growth process, using the reduced order surface kinetics model, replicates these features.

Looking at the fine structure (in the PR75 data), the most noticeable change with the TEG pulse position variation is the starting position of the downward slope (near the arrows marked in the Fig. 5) which is present in every data set but moves to later in the cycle as the TEG pulse moves to later in the cycle. This start of the downward slope, which is the only feature so dependent on the TEG pulse placement, clearly relates to the source TEG, the subsequent TEG defragmentation and active gallium attachment on the surface.

In contrast, the starting position of the upward slope in the fine structure remains in the same place shortly after the start of the cycle, independent of the TEG pulse position. It can be related to the source TBP exposure, its defragmentation and the formation of active phosphorus on the surface.

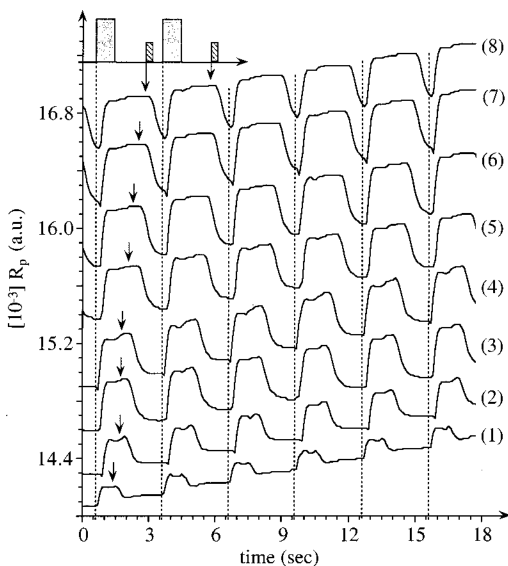

FIG. 8. Simulated PR75 responses for various TEG positions within a cycle sequence, with the rest of the source cycle properties kept constant. These properties and the location shown match those of the experimental data in Fig. 5. The changed TEG starting point is marked by an arrow.

Both starting positions are delayed by approximately 0.72 s after the start of the pulses. This delay is due to the time needed to open the source vapor gates and the time for the vapors to travel to the surface, as noted in the description of the model.

The same upward and downward slopes and delay characteristics can be seen in Fig. 8, where the fine structure evolutions of the simulated data are compared at the same points as the experimental data in Fig. 5. The gap between the downward and upward slopes can be analyzed by the full width at half maximum (FWHM), defined by the width between times on the downward and upward slopes with values halfway between the maximum and minimum reflectance during that cycle. Figure 9 illustrates how this width shrinks as the TEG pulse is moved toward the end of the cycle and closer to the next TBP pulse. This change, in both the experimental and calculated data, follows the pulse position nearly linearly.

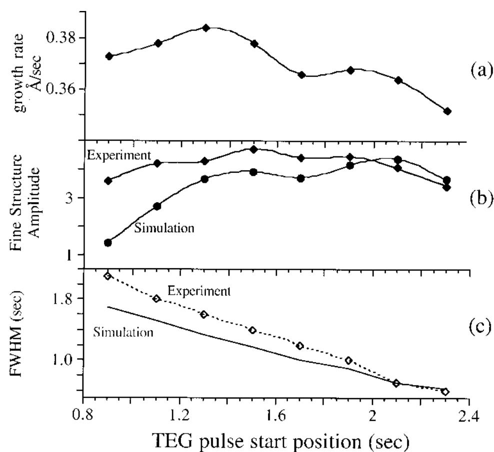

FIG. 9. Properties of the PR responses as affected by the TEG start position: (a) average film growth rate; (b) amplitude of the fine structures in Figs. 5 and 8; and (c) FWHM of the fine structures.

The fine structure amplitude (the difference between the maximum and minimum reflectance over a cycle) also changes slightly but clearly with the change in TEG pulse position. As shown in Fig. 9, the amplitude is largest for TEG pulses near the middle of the range used. This can be explained as a result of the closeness of the TEG and TBP pulses. If the TEG is input soon after the TBP, there will be a large GaP formation reaction, leaving little or no active gallium to carry over to the next cycle. If the TEG comes in very late in the cycle, right before the next TBP pulse, there may not be time for decomposition of all the TEG to gallium to occur before GaP formation with the incoming phosphorus starts. With a more central TEG pulse, the phosphorus and gallium will each have the time to build up on the surface, in turn creating more extreme changes in the SRL thickness and composition and therefore larger fine structure amplitude.

Note that this analysis of the fine structure is at a specific place on the interference oscillations, fairly high on a rising flank. Other places, particularly on the other side of a turning point, will have different characteristics (for example, the TEG pulse may result in a jump upward and the TBP pulse in a jump downward).

One larger-scale feature of the reflectance data we can look at is the average film growth rate for the various TEG pulse positions, shown in Fig. 9. The general downward slope can be explained in terms of the closeness of the two pulses. As the TEG pulse moves later in the cycle away from the TBP pulse there is less phosphorus to react with, so there is more active gallium left on the surface to be lost via desorption. The TEG pulse positions nearest the start of the cycle seem to be too close to the TBP pulse for the fastest growth rate however. The incoming TEG and its defragmentation products may be partially blocked from the available active phosphorus in the SRL by TBP that failed to stick and/or desorbed phosphorus that is sitting loose on the surface.

Another large-scale characteristic feature of the data sets is the position of (or complete lack of) turning points in the fine structure. These come in pairs for every interference oscillation or not at all, as discussed in Sec. IV (with a closeup of a turning point in Fig. 7). The turning point positions can be characterized by the derivative of the reflectance. The overall derivative amplitude is related to the periodic thickness changes in the SRL. This amplitude is minimized at the turning points, where the fine structure amplitude is smallest and so the reflectance curve least steep. Figure 10 shows the close match between the experimental and calculated derivative amplitudes and turning point positions. In earlier works,[5,6] we showed that the locations of these turning points change as a function of the SRL dielectric properties. The good agreement shown in Fig. 10 indicates that the SRL dielectric properties were obtained correctly.

The measurements taken with the TEG pulse position fixed but the flow rate varied also correspond to what is expected. Examples of the fine structure (again for PR75) for the three TEG flow rates are shown in Fig. 11 for both ex-

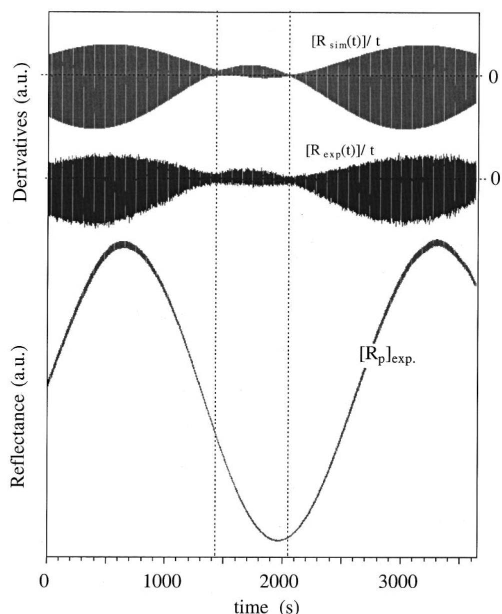

FIG. 10. Characterization of the fine structure envelope using the first derivative of the reflectance spectrum. For comparison, the experimental and simulated reflectance spectra with their (numerical) first derivatives are shown (TEG pulse is 1.3–1.6 s). The simulated reflectance spectrum lies on top of the experimental spectrum and is not shown for clarity.

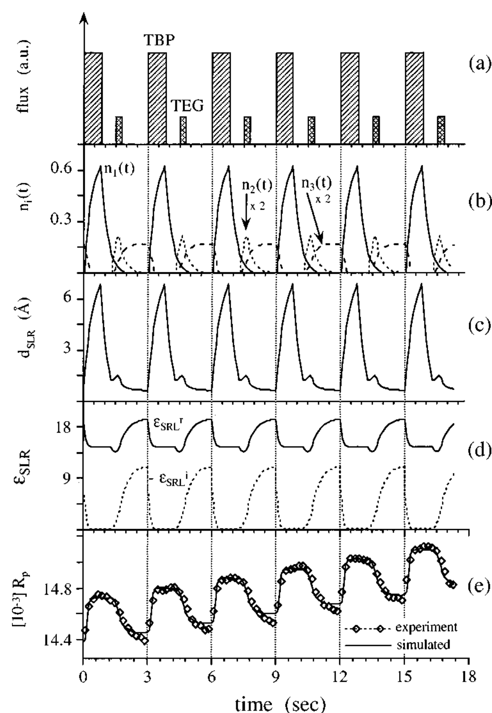

FIG. 12. Contributions of parts of the model to the simulated reflectance: (a) source vapor fluxes, (b) number of moles of the three SRL components, (c) SRL thickness, and (d) SRL effective dielectric function real and imaginary parts. These result in (e) simulated PR response, showing experimental fitting measurements (for TEG 1.3–1.6 s).

perimental data and simulated data. In contrast with the variation of the pulse position, here the shape of the fine structure remains the same, since the shape of the source vapor cycle is the same. The positions of changes in the slope remain constant due to the constant position of the TEG pulse. The amplitude of the fine structure does change, since as the TEG flow rate increases there will be more gallium deposited in the SRL, and this will cause a larger effect in the reflectance. Larger TEG flow also results in a much faster film growth rate, which causes steeper large-scale curves as seen in Fig. 11 and faster interference oscillations as seen in Fig. 6. Both the experimental and simulated data sets show these characteristics and both results agree with each other extremely well.

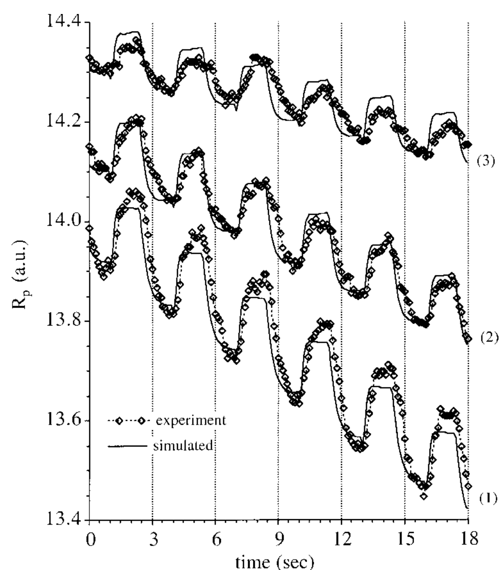

FIG. 11. Experimental and simulated PR75 responses for various TEG fluxes under steady-state growth conditions. The TBP exposure time, position and flux were kept constant, as were the surface exposure time and pulse position for TEG. The TEG fluxes used were (1) 0.05, (2) 0.04 and (3) 0.03 sccm.

The steps in the generation of a set of simulated data which were used to compare against experimental data presented in Fig. 3 are shown in detail in Fig. 12 for a TEG pulse of 1.3–1.6 s (and a TBP pulse of 0.0–0.8 s). The three SRL components are the result of the source pulses and ROSK model simulation. From the SRL components, the SRL thickness and dielectric function are found. These values then contribute to the calculated reflectance. Figure 12 shows how the arrival of gallium in the SRL causes the downward slope in the fine structure and how the arrival of phosphorus causes the upward slope. The good fit of this simulated fine structure to the experimental data as shown in Fig. 12 will also hold for the rest of the interference oscillations. This is illustrated in Fig. 10, where the reflectance derivatives match, as the actual reflectance curves match (and the fine structure amplitudes and turning points also agree). The closeness of the fit and the correlation of the significant features discussed above support the ROSK model of the growth process and its effects on the reflectance measurements.

An important aspect of the behavior of the SRL kinetics which can be seen in Fig. 12 is the difference between a phosphorus- and gallium-terminated surface at the end of a cycle sequence. We had at first expected a phosphorus-terminated surface at the end of each cycle sequence time,

where the TEG pulse is almost completely used up through desorption or formation of GaP, leaving some phosphorus in the SRL at the start of the next pulse cycle. However, simulated reflectance data with this type of behavior could not fit the experimental data. Instead, a set of parameters which resulted in a gallium-terminated surface (where the TEG pulse is not all used up at the end of the cycle time, leaving an amount of gallium in the SRL being carried over to the next cycle) gave a much more accurate fit as described above.

The data measured at the second angle (PR70) have structures and features similar to the PR75 data, with the major difference being the inversion of interference oscillation maxima/minima since the angles are on opposite sides of the pseudo-Brewster angle. Analysis of these measurements using the same model results in parameters similar to those found for PR75 (which are given below) and a similar fit of the reflectance data. There are a few noticeable differences between the two, which can be explained by the measurements being taken with light beams hitting different points on the surface. If the growth is somewhat uneven this could cause differences in the parameters in the growth model when the two data sets are compared.

The values used in the calculations of the model are as follows. The molar volumes used in the minimization process were $V_{TBP}=128.6\ cm^3\,mol^{-1}$, $V_{TEG}=148\ cm^3\,mol^{-1}$, $V_1=17\ cm^3\,mol^{-1}$, $V_2=13\ cm^3\,mol^{-1}$, $V_3=11.8\ cm^3\,mol^{-1}$, and $V_{GaP}=12.2\ cm^3\,mol^{-1}$. The sticking coefficients used were $\beta_{TBP}=0.15$ and $\beta_{TEG}=1.0$, and the effective SRL thickness parameter $\alpha_{SRL}=0.75$. The geometrical parameter $\gamma=0.025$ was estimated in the minimization process for a 2 in. diam circular substrate wafer.

The numerical simulations were done using programs written in MATLAB code. The differential equations were solved numerically by the built-in function ''ode23,'' an adaptive mesh and low order Runge-Kutta method, and the optimization problem was solved using either a Nelder-Mead algorithm[24–26] or a Hooke-Jeeves procedure.[24] We estimated the following parameters by averaging the results of independent best fits of experimental data sets when the TEG position and TEG flow were varied. The preliminary three-layer stack problem resulted in $\epsilon_3=10.60-0.06i$ and $\epsilon_4=15.82-0.27i$. Using these, the parameter estimation results from the four-layer stack model gave the following parameter values: rate constants of $k_1=3.31\ s^{-1}$, $k_2=1.55\ s^{-1}$, $k_3=2.14\ s^{-1}$, $k_4=0.052\ s^{-1}$ and $k_{GaP}=2.0\ mol^{-1}\ s^{-1}$; optical responses of $F_1=13.46-0.13i$, $F_2=13.56-0.0i$ and $F_3=19.36-11.02i$. These parameters produce an average SRL dielectric function of $16.82-4.47i$ and an average film growth rate of 0.365 Å/s. An earlier study on the decomposition kinetics of TEG, analyzing the PR responses to a TEG exposure after growth interruptions,[12] gave rate constants of $k_3=0.4\ s^{-1}$ and $k_{GaP}=0.24\ s^{-1}$. The higher value for k_{GaP} was expected since no thermally activated hydrogen was employed to the growth surface and the flow rates were lowered by a factor of about 2 in our experiments.

VI. CONCLUSIONS

We introduced a reduced order surface kinetic model using generalized reaction rate parameters to describe the decomposition kinetics of the organometallic precursors TBP and TEG used during heteroepitaxial growth of GaP on Si. The set of coupled differential equations that describe the surface reaction kinetics provide information about the dynamics of molar concentrations of precursor fragments stored in the surface reaction layer and their incorporation into the underlying growing film. We fitted sets of experimental data using this model to identify the unknown parameters involved in the surface kinetics and their effect on the PR measurements. The results showed that the mathematical model can be used to effectively predict the large- and small-scale features of the experimental data and to model the deposition process. However, a validation of the predicted surface reaction layer constituents and their concentrations, as computed by the ROSK model, will require the development of highly surface-sensitive, molecular specific diagnostic techniques that allow analysis of the dynamics in the SRL under steady-state growth. For this, the application of PRS in the infrared wavelength regime, using tunable laser sources, has been proposed.

ACKNOWLEDGMENTS

The authors are indebted to Professor K. J. Bachmann for helpful comments and suggestions. The authors are grateful to Professor Kelley for providing them with the code ''nelder'' implementing the Nelder-Mead algorithm and to Mr. D. Bortz who provided them with the code ''*hj*'' implementing the Hooke-Jeeves procedure, which was used in some optimization calculations. Both Professor Kelley and Mr. Bortz are at the Department of Mathematics, North Carolina State University. The authors acknowledge support for this work by DOD-MURI Grant No. F49620-95-1-0447.

[1] See, for example, Conference Proceedings of IPRM-9 '97, ISSN 1092-8669 (1997).
[2] Proceedings of DARPA Ultra Electronics and Advanced Microelectronics Program Review, Santa Fe, NM, 26–31 October 1997.
[3] D. E. Aspnes and N. Dietz, Appl. Surf. Sci. **130–132**, 367 (1998).
[4] N. Dietz and K. J. Bachmann, MRS Bull. **20**, 49 (1995).
[5] N. Dietz and K. J. Bachmann, Vacuum **47**, 133 (1996).
[6] N. Dietz, N. Sukidi, C. Harris, and K. J. Bachmann, J. Vac. Sci. Technol. A **15**, 807 (1997).
[7] N. Dietz and K. Ito, Thin Solid Films **313–314**, 615 (1998).
[8] N. Dietz, A. Miller, and K. J. Bachmann, J. Vac. Sci. Technol. A **13**, 153 (1995).
[9] N. Dietz, A. Miller, J. T. Kelliher, D. Venables, and K. J. Bachmann, J. Cryst. Growth **150**, 691 (1995).
[10] N. Dietz, U. Rossow, D. Aspnes and K. J. Bachmann, J. Electron. Mater. **24**, 1571 (1995).
[11] K. J. Bachmann, N. Dietz, A. E. Miller, D. Venables, and J. T. Kelliher, J. Vac. Sci. Technol. A **13**, 696 (1995).
[12] K. J. Bachmann, U. Rossow, N. Sukidi, H. Castleberry, and N. Dietz, J. Vac. Sci. Technol. B **14**, 3019 (1996).
[13] N. Dietz, U. Rossow, D. E. Aspnes, and K. J. Bachmann, Appl. Surf. Sci. **102**, 47 (1996).
[14] N. Dietz, U. Rossow, D. E. Aspnes, and K. J. Bachmann, Appl. Surf. Sci. **102**, 47 (1996).
[15] K. J. Bachmann, N. Sukidi, N. Dietz, C. Hoepfner, S. LeSure, H. T. Tran, S. Beeler, K. Ito, and H. T. Banks, J. Cryst. Growth **183**, 323 (1998).
[16] N. Dietz, N. Sukidi, C. Harris, and K. J. Bachmann, in Ref. 1, p. 521.
[17] K. J. Bachmann, C. Hoepfner, N. Sukidi, A. E. Miller, C. Harris, D. E.

Aspnes, N. Dietz, H. T. Tran, S. Beeler, K. Ito, H. T. Banks, and U. Rossow, Appl. Surf. Sci. **112**, 38 (1997).
[18] O. S. Heavens, *Optical Properties of Thin Solid Films* (Butterworths, London, 1955).
[19] L. Ward, *The Optical Constants of Bulk Materials and Films*, 2nd ed. (IOP, London, 1994).
[20] S. H. Li, C. A. Larsen, N. I. Buchan, G. B. Stringfellow, W. P. Kosar, and D. W. Brown, J. Appl. Phys. **65**, 5161 (1989).
[21] G. H. Fan, R. D. Hoare, M. E. Pemble, I. M. Povey, A. G. Taylor, and J. O. Williams, J. Cryst. Growth **124**, 49 (1992).
[22] A. J. Murrell, A. T. S. Wee, D. H. Fairbrother, N. K. Singh, J. S. Foord, G. J. Davies, and D. A. Andrews, J. Cryst. Growth **105**, 199 (1990).
[23] G. Burns, *Solid State Physics* (Academic, Orlando, 1985), p. 461.
[24] C. T. Kelley, SIAM (1999).
[25] C. T. Kelley, Center of Research in Scientific Computation, North Carolina State University, CRSC-TR97-2 (1997).
[26] D. M. Bortz and C. T. Kelley, in *Computational Methods in Optimal Design and Control*, Progress in Systems and Control Theory, edited by J. T. Borggaard, J. Burns, E. Cliff, and S. Schreck (Birkhäuser, Boston, 1998), p. 77.